Ultrafast Charge Carrier Dynamics in Vanadium-Modified TiO$_2$ Thin Films and Its Relation to Their Photoelectrocatalytic Efficiency for Water Splitting

Alberto Piccioni, Daniele Catone, Alessandra Paladini, Patrick O'Keeffe, Alex Boschi, Alessandro Kovtun, Maria Katsikini, Federico Boscherini,* and Luca Pasquini

Read Online

ACCESS | Metrics & More | Article Recommendations | SI Supporting Information

ABSTRACT: Light absorption and charge transport in oxide semiconductors can be tuned by the introduction, during deposition, of a small quantity of foreign elements, leading to the improvement of the photoelectrocatalytic performance. In this work, both unmodified and vanadium-modified TiO$_2$ thin films deposited by radio-frequency magnetron sputtering are investigated as photoanodes for photoelectrochemical water splitting. Following a structural characterization by X-ray diffraction, atomic force microscopy, Raman spectroscopy, and X-ray photoelectron spectroscopy, photoelectrocatalysis is discussed based on ultrafast transient absorbance spectroscopy measurements. In particular, three different pump wavelengths from UV to the visible range are used (300, 390, and 530 nm) in order to cover the relevant photoactive spectral range of modified TiO$_2$. Incident photon-to-current conversion efficiency spectra show that incorporation of vanadium in TiO$_2$ extends water splitting in the visible range up to $\approx$530 nm, a significant improvement compared to unmodified TiO$_2$ that is active only in the UV range $\lesssim$390 nm. However, transient absorbance spectroscopy clearly reveals that vanadium accelerates electron–hole recombination upon UV irradiation, resulting in a lower photon-to-current conversion efficiency in the UV spectral range with respect to unmodified TiO$_2$. The new photoelectrocatalytic activity in the visible range is attributed to a V-induced introduction of intragap levels at $\approx$2.2 eV below the bottom of the conduction band. This is confirmed by long-living transient signals due to electrons photoexcited into the conduction band after visible light (530 nm) pulses. The remaining holes migrate to the semiconductor–electrolyte interface where they are captured by long-lived traps and eventually promote water oxidation under visible light.
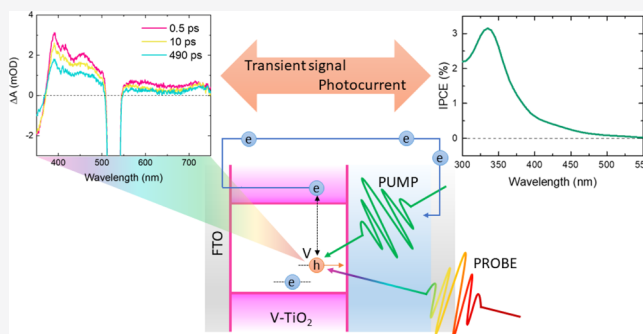
INTRODUCTION

A great deal of research has been performed on titanium dioxide (TiO$_2$) since the 1960s with the aim to improve its photocatalytic properties and to understand the underlying atomistic mechanisms.[1−5] Thanks to its numerous advantages such as good charge transport,[6] stability in aqueous environments, and photostability, TiO$_2$ has found extensive applications in the fields of photocatalysis and photoelectrocatalysis.[7] For example, the photocatalytic properties of TiO$_2$ nanoparticles have been exploited to develop advanced oxidative processes for water treatment, while TiO$_2$-based electrodes have been developed for a number of photoelectrocatalytic reactions such as water splitting[8,9] and CO$_2$ reduction.[10] However, the widespread growth of these applications has been limited by the wide energy gap of TiO$_2$ (3.2 eV for the anatase polymorph), which only allows efficient absorption of UV light, that is, ca 5% of the full solar spectrum. The result is a poor solar-to-hydrogen conversion efficiency and an almost vanishing photocatalytic activity indoor.

The limited efficiency of TiO$_2$ in the visible range has triggered the search for methods to improve it, including dye sensitization,[11] use of plasmonic/TiO$_2$ structures,[12,13] semiconductor heterostructures[14] and doping with both metals and nonmetals.[15] In this work, we concentrate on extending light absorption of TiO$_2$ thin films into the visible range via vanadium incorporation (referred to as V−TiO$_2$ in the following). Previously,[16−18] we used vanadium as a dopant in TiO$_2$ nanoparticles deposited by inert gas condensation. We found the incorporation site of vanadium to be substitutional to titanium, with both 4+ and 5+ oxidation states;[17] V-incorporation induces the creation of intragap localized donor

levels,[19] which lead to a red shift of optical absorption, also in agreement with a recent computational work by Zhou et al.[20] The nanoparticles were deposited on a conductive substrate to obtain nanostructured and porous photoanodes used in a photoelectrochemical cell (PEC) for water splitting or were suspended in a solution for photocatalytic conversion of organic compounds. The use of nanostructured photoanodes brings benefits in terms of efficiency, thanks to the increased surface-to-volume ratio, but, on the other hand, charge transport properties of the material can be detrimentally affected. In the present work, we study the properties of homogeneous V-modified TiO_2 thin films, as opposed to nanostructured porous films, with the objective of studying the response of the bulk material, excluding the effect of other variables such as the morphology and surface-to-volume ratio.

Fast transient absorbance spectroscopy (FTAS) is a very powerful method, which can help to correlate the photo-electrocatalytic efficiency and charge carrier dynamics; it can exhibit very high temporal resolution (down to tens of femtoseconds) and can separately probe the transient dynamics of electrons and holes, thanks to the wide spectral range (from UV to IR).[21] The identification of transient signals due to specific charge carriers and relaxation pathways has been reported in several studies in past years.[22−27] In general, three main spectroscopic signatures are observed in TiO_2, ascribed to trapped holes (THs), trapped electrons, and free electrons (as described in the Drude−Lorentz model). Schneider et al.[5] summarized the results concerning THs and electrons: the maximum of the TH signal is found in the range from 400 to 630 nm, while the maximum of the trapped electron signal is in the range from 620 to 2500 nm. The position of the maxima is strongly affected by the use of different holes or electron scavengers. On the other hand, free electrons do not give rise to peaks in FTAS spectra but generate a monotonically increasing background, which extends from the visible to the IR region with a power-law dependence on the wavelength. These assignments have been recently confirmed by ab initio methods.[28]

In this work, we used FTAS to study the charge carrier dynamics in V−TiO_2 thin films. The results are related to the photoelectrochemical efficiency of water splitting measured when the films are employed as photoanodes. In order to determine the dynamics of the charge carriers, we propose a data fitting procedure that takes into account thin-film interference effects, which modulate the transient spectra leading to overlapped electrons and hole signals. We show the benefits of vanadium modification in extending both the optical absorption and photoelectrochemical activity of TiO_2 in the visible range, where it is normally inactive.

■ EXPERIMENTAL SECTION

TiO_2 and V−TiO_2 thin films were deposited by radiofrequency magnetron sputtering in an ultrahigh-vacuum chamber previously evacuated to 10^{-7} mbar. The sputtering gas was pure argon (99.999%) at a pressure of 8×10^{-3} mbar, which was dynamically maintained using a mass flow controller and controlled pumping. The power supplied to the TiO_2 target was kept constant at 75 W throughout the deposition process. For the deposition of V−TiO_2 films, small rectangular vanadium pieces were attached with carbon tape on the edge of the TiO_2 target, as shown in Figure S1 of the Supporting Information. Three levels of V concentration were investigated, corresponding to atomic ratios V/(Ti + V) = 4, 6, and 8 at. %. Accordingly, the samples will be indicated as V−TiO_2 (x %) with x = 4, 6, or 8.

Two kinds of substrates were used for the deposition: a soda lime glass coated by a 200 nm thick layer of fluorine-doped tin oxide (FTO) purchased from Ossila for photoelectrochemical measurements and quartz (from Electro-Optics Technology) for FTAS experiments. Film thicknesses ranged from 50 to 170 nm. The determination of the thickness was carried out by exploiting a calibration procedure based on scanning electron microscopy, which indicated a linear dependence of the thickness on the evaporation time with a rate of 1.7 nm/min. Unless otherwise noted, the results reported in this paper are relative to films that were annealed at 400 °C in air for 16 h in order to improve the crystallinity. The amount of vanadium was estimated by energy-dispersive X-ray spectroscopy (EDS) using a Leica Cambridge Stereoscan 360 scanning electron microscope equipped with an Oxford Instruments X-ray detector for energy-dispersive X-ray microanalysis.

X-ray diffraction (XRD) patterns were recorded employing a PANalytical X'Pert Pro automated diffractometer equipped with an X'celerator multielement solid-state detector. The diffractometer was operated in Bragg−Brentano $\theta/2\theta$ para-focusing geometry using Ni-filtered Cu Kα radiation without a monochromator in the diffracted beam. X-ray photoelectron spectroscopy (XPS) was carried out by a Phoibos 100 hemispherical energy analyzer (Specs GmbH) using non-monochromatized Mg Kα radiation (photon energy $\hbar\omega$ = 1253.6 eV and an overall resolution of ∼0.9 eV); energy calibration was performed by using the Ag $3d_{5/2}$ core level emission from a freshly Ar$^+$-sputtered silver sample. The Raman spectra were recorded in backscattering geometry using a DILOR-XY spectrometer equipped with an optical microscope and a 100× objective. The green line (514.5 nm) of an Ar$^+$ laser was used for the excitation. The spectra were calibrated utilizing a neon lamp. The morphology of the semiconductor surface was evaluated on a Park Systems NX10 atomic force microscope in a noncontact mode using a PPP-NCHR (Nanosensors) cantilever.

The spectral efficiency of the photoanodes for water splitting was determined in a PEC cell using a three-electrode configuration with a Pt counter electrode and a saturated calomel electrode (SCE) as the reference. The electrolyte was a 0.1 M KOH solution (pH = 13) and a bias potential of 0.5 V versus SCE was applied to facilitate charge collection. The photoanodic current was recorded using a PGSTAT204 electrochemical workstation as a function of the incident wavelength from 300 to 600 nm in steps of 5 nm. The PGSTAT204 output signal, proportional to the photoanodic current, was fed into a lock-in amplifier and the incident light was chopped at 2 Hz. The light source was an Osram 150 W xenon arc lamp and the incident monochromatic irradiance was measured with a calibrated pyroelectric sensor. The incident photon-to-current conversion efficiency (IPCE) was calculated using

$$\text{IPCE (\%)} = 1.24 \times 10^3 J_\lambda (\mu A \cdot cm^{-2})/[\lambda(nm) \cdot P_\lambda(Wm^{-2})] \tag{1}$$

in which J_λ and P_λ are the photocurrent density and incident radiant power density, respectively, at wavelength λ.

FTAS measurements were performed in a pump−probe configuration with a laser system consisting of an 80 MHz Ti:Sa oscillator (Coherent Vitara-T) that seeds a chirped pulse amplifier with broadband 800 nm (fwhm 100 nm) pulses of 12.5 nJ. The amplifier produces 4 mJ 35 fs pulses at a repetition rate of 1 kHz. A part of this radiation is used to generate 40 fs pump

pulses of different wavelengths (λ_e = 300, 390, and 530 nm) in an optical parametric amplifier (Coherent–Opera Solo) at a repetition rate of 1 kHz. A white light probe pulse (λ_p = 350 − 760 nm) was generated in a commercial FTAS spectrometer (FemtoFrame II, IB Photonics) by focusing 3 μJ of the 35 fs 800 nm light into a rotating 3 mm crystal of CaF$_2$. We employ a split beam configuration, in which 50% of the white light passes through the sample, while the remainder is used as a reference to account for pulse-to-pulse fluctuations. The pump pulse is loosely focused (circular spot with a diameter of 300 μm) onto the sample with an energy density of 100 μJ/cm^2 for λ_e = 300 and 2 mJ/cm^2 for λ_e = 390 and 530 nm. The diameter of the probe pulse is much smaller (approx. 150 μm), and its delay time with respect to the pump pulse is scanned in time by varying the length of its optical path. The instrument response function (IRF) was measured to be approximately 80 fs (see the Supporting Information). All measurements were performed in air at room temperature in the transmission mode. Further details of the setup can be found in ref 29. The FTAS spectra $\Delta A(\lambda, t)$ are defined as the difference in absorbance between the excited state at time t and the ground state at time t_0, according to

$$\Delta A(\lambda, t) = \log_{10} \frac{I_{gnd}(\lambda, t_0)}{I_{exc}(\lambda, t)} \qquad (2)$$

where $I_{gnd}(\lambda, t_0)$ is the transmitted intensity before the pump pulse and $I_{exc}(\lambda, t)$ is the transmitted intensity at the delay time t after excitation.

■ RESULTS AND DISCUSSION

Structural and Surface-Chemical Characterization. XRD was used to identify the crystallographic phases present in the samples and the changes induced by V incorporation. In Figure 1 we report XRD patterns for the glass FTO substrate,
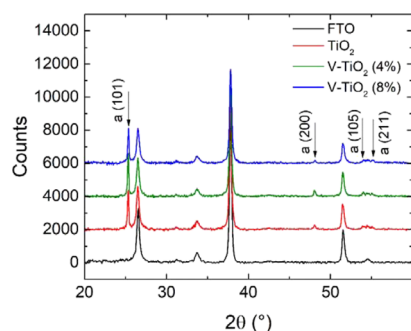

Figure 1. XRD patterns of the glass FTO substrate, unmodified TiO$_2$, and V–TiO$_2$ films. The detected Bragg reflections of anatase TiO$_2$ are indexed; the other peaks come from the FTO substrate.

unmodified TiO$_2$, and V–TiO$_2$ (4 and 8%) films. The patterns are dominated by the Bragg reflections arising from the FTO substrate. In addition, the (101) diffraction peak at $2\theta \approx 25.3$, typical of anatase TiO$_2$ (space group $I4_1/amd$, lattice parameters a = 3.783 Å, c = 9.510 Å), is clearly visible in all samples. The other reflections of anatase are much weaker than expected for an isotropic distribution of crystallite orientations or even not visible, indicating that the films are textured with the (101) planes parallel to the surface. The other common polymorphs of TiO$_2$, that is, rutile and brookite, are not detected. The positions of diffraction peaks are the same for all samples within the experimental uncertainty, indicating that the lattice parameters

vary less than 0.1% with the V concentration. This is expected at low V contents given the similar atomic radius of the two elements. The d-spacing of the (101) planes is reported in Table S1 of the Supporting Information as a function of composition and for different thicknesses at the highest V content.

The full width at half-maximum (FWHM) of the (101) peak is about 0.16°, compared to an instrumental FWHM of 0.12°, and shows small variations with the composition. Such a small broadening implies a large uncertainty in the determination of the crystallite size. The values obtained using Scherrer's equation (taking into account the instrumental FWHM) are reported in Table S1 of the Supporting Information. The crystallite size ranges between 80 and 100 nm for all samples, the only exception being the thinnest V–TiO$_2$ (8%) film, where the crystallite size is about 60 nm. This result is consistent with the reduced thickness because XRD measures the elongation of the diffracting column in a direction perpendicular to the surface. The crystallite size values should be considered as lower-bound estimates because other factors, such as the root-mean-square microstrain, may contribute to the broadening of Bragg peaks.

In Figure 2 (left), an AFM topography of the surface of a V–TiO$_2$ (8%) photoanode is shown (with FTO as the substrate), while on the right of the same figure, the surface of a similar sample deposited on quartz for FTAS measurements is reported. No relevant differences were found between V-modified and unmodified TiO$_2$ samples. In photoanodes, two different structures are visible: one is clearly induced by the morphology of the FTO surface (red circle) and is not present on the sample deposited on quartz and the other (green circle) is attributed to TiO$_2$ crystal grains, with a lateral size of 27 ± 5 nm. The latter structure is also present on the surface of TiO$_2$ deposited on quartz, with a lateral size of 24 ± 5 nm. The roughness of the two films is 16.1 ± 2.7 nm for photoanodes and 3.7 ± 0.4 for TiO$_2$ on quartz. The higher roughness of the photoanodes reflects the high roughness of the underlying FTO substrate. The roughness of the quartz substrates is only 0.7 ± 0.2 nm; therefore, the observed film roughness likely originates from columnar grains of slightly different heights, which is typical of sputter-deposited films.

The Raman spectra of the films are shown in Figure 3. Four peaks, at 144, 395, 515, and 636 cm^{-1} corresponding to the E_g, B_{1g}, B_{1g}/A_{1g}, and E_g normal modes, respectively, are evident. They are characteristic of the anatase polymorph, while peaks due to rutile were not detected.[30] Table S2 in the Supporting Information lists the positions and the FWHM of the most intense $E_g(\nu_6)$ peak, which was determined after fitting with a Lorentzian function. The FWHM values indicate a good crystalline quality of the films. With the increasing V content, both a broadening and a blue shift $\Delta\omega = \omega - \omega_0$ of the peak (relative to the corresponding value for bulk anatase, $\omega_0 = 144$ cm^{-1}) are observed. A blue shift of the $E_g(\nu_6)$ Raman mode was reported for anatase films grown on different substrates.[31] It was linearly correlated with the stress (and strain) in the films, as calculated from the variation of the lattice parameters determined by XRD. According to the data of Alhomoudi[31] and Newaz, a blue shift of ~2 cm^{-1}, as listed in Table S2 for V-modified samples, would correspond to a compressive strain of ~0.6%. In the present case, however, XRD suggests that the variation of the lattice parameters among different samples is below 0.1%. Therefore, other V-related factors must be responsible for the observed blue shift of the Raman spectral features. We note that similar blue shifts were previously reported for anatase films deposited on glass substrates at 350
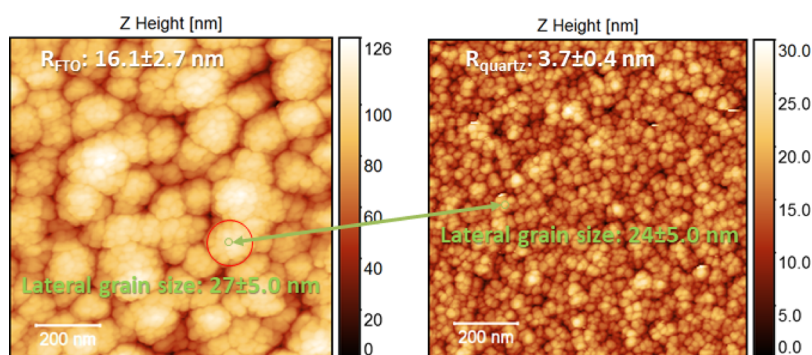
Figure 2. Surface morphology of V−TiO$_2$ (8%) photoanodes on FTO (left) and V−TiO$_2$ (8%) on quartz (right).
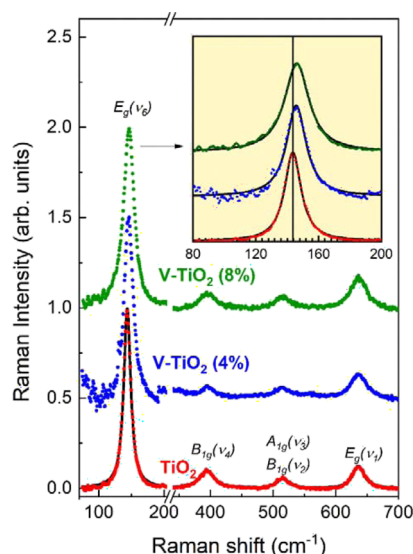

Figure 3. Raman spectra of the unmodified and V-modified TiO$_2$ samples. The colored symbols correspond to the experimental spectra. A representative fitting using Lorentzian lineshapes is shown in the case of the unmodified sample. The inset shows magnification of the spectra around the main $E_g(\nu_6)$ peak along with the corresponding fitting. The vertical line denotes the position of the $E_g(\nu_6)$ peak of the unmodified sample.

°C; they were attributed to local distortions and to the presence of bonds with different force constants, arising from the incorporation of substitutional V^{4+} cations in the Ti sublattice.[32]

These factors may also contribute to the V-induced broadening of Raman features, which is in qualitative agreement with the broadening of the (101) Bragg peak observed at the highest V incorporation level. The incorporation of V in the TiO$_2$ lattice leads to an increased disorder and to a distribution of bond strengths, which appears to enhance phonon scattering. Size effects as a genuine broadening mechanism can be excluded because they should also induce a peak asymmetry, which is not observed here, and they become evident for a crystallite size smaller than 20 nm, well below the XRD estimate discussed above.[33]

XPS was used to quantify the V content in the surface region and to probe its oxidation state. We note that these measurements probe the surface region of the films, which plays the most important role in charge transfer at the semiconductor−electrolyte interface. We believe that these ex situ measurements on the air-exposed and ready-for-use photoanode, rather than in situ ones during film growth, are

the most relevant to relate the near-surface atomic and electronic structure of the materials to the functional properties of the photoanode. Ex situ XPS measurements were performed on both pristine and annealed unmodified TiO$_2$ and V−TiO$_2$ (6%) films. The spectra exhibit contributions because of O 1s, V 2p, and Ti 2p core levels along with a C 1s contribution originating with adventitious C due to air exposure.[34−36] A description of the line shapes of the Ti, O, and C core level signals and details on the XPS data analysis are reported in the Supporting Information. The intensity of Ti, V, and O signals indicates, as expected, an O/(Ti + V) ratio of 2.0 ± 0.2. In Figure 4, we report

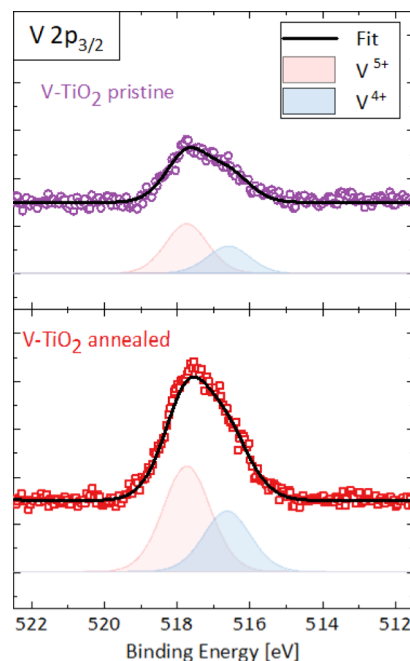**Figure 4.** V 2p$_{3/2}$ XPS spectra of the V−TiO$_2$ (6%) film before (top) and after (bottom) annealing. Empty symbols: background-subtracted experimental spectra; continuous lines: fits; filled contours: V^{4+} and V^{5+} fitting components.

V 2p$_{3/2}$ XPS spectra for the pristine and annealed V−TiO$_2$ (6%) films. By comparing its intensity with that of Ti, we can quantify the V concentration [calculated as V/(Ti + V)] in the surface layer probed by XPS (a few nanometers). For the pristine film, we found a V concentration of 6 ± 1%, in agreement with the EDX determination. Instead, annealing leads to a significant increase of the V concentration to 16 ± 2%, indicating that thermal treatment promotes the migration of V atoms toward

the surface. The line shape reported in Figure 4 clearly exhibits two components, which were decomposed by a fitting procedure (see the Supporting Information).

By comparing the binding energies of the two components (516.6 and 517.7 eV), which do not change upon annealing, to those reported by Silversit et al.,[37] we conclude that V is found in both 4+ and 5+ oxidation states. The fraction of V^{4+} was 0.38 ± 0.10 in the pristine sample and 0.32 ± 0.10 in the annealed sample. These numbers clearly refer to the surface of the films, as XPS is very surface-sensitive. Bulk-sensitive X-ray absorption spectroscopy experiments carried out on similar films suggest a dominant presence of V^{4+} substitutional cations in the inner layers.[32]

Photoelectrochemistry. IPCE spectra are reported in Figure 5 for two V−TiO₂ incorporation levels and a range of film
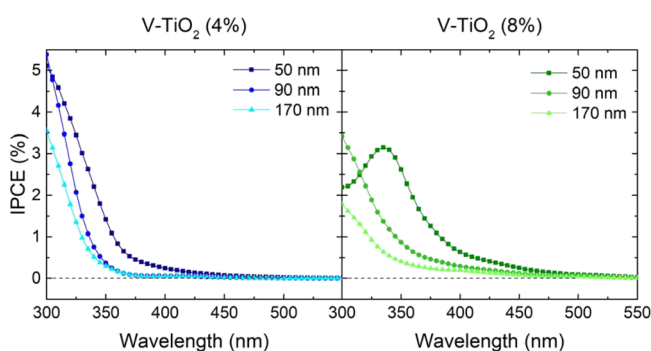

Figure 5. IPCE spectra of V−TiO₂ films (4 and 8%) for different film thicknesses.
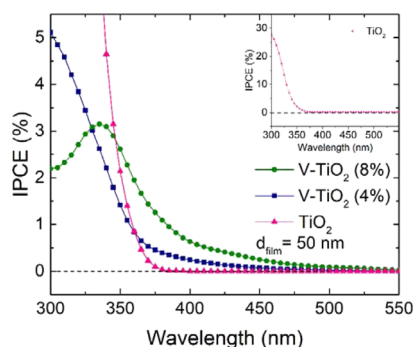

Figure 6. Comparison between IPCE spectra of V-modified and unmodified TiO₂ thin films with a fixed film thickness ($d = 50$ nm). The inset displays the full IPCE curve for TiO₂.

thicknesses. In Figure 6, we compare IPCE spectra of unmodified and modified films for a constant film thickness of 50 nm. In discussing these spectra, it is useful to distinguish two spectral ranges: the visible range for wavelengths longer than 390 nm and the UV range for wavelengths below 390 nm. Three main features can be highlighted in these spectra, which will be related to the results from FTAS measurements in the next section.

    i   There is a decrease of IPCE in both UV and visible ranges with increasing film thickness. This is most likely due to the longer path that electrons have to travel through the bulk before reaching the FTO substrate, which increases the recombination probability of the charge carriers and

hence reduces the collected current. We note that the IPCE curve for the 8% modified 50 nm film exhibits a peak at about 340 nm. This feature can be understood considering the effect of the limited thickness (comparable to the attenuation length for UV radiation) combined with the enhanced recombination rate at high V incorporation that will be discussed later.

    ii   The overall photoelectrocatalytic activity in the UV range decreases with V incorporation.

    iii   The photoelectrocatalytic activity in the visible range (up to ≈550 nm) is higher for the 8% modified sample than for the 4% modified sample. The unmodified sample is completely inactive in this spectral range, as evident from Figure 6.

In the Supporting Information, we report electrochemical impedance spectroscopy and cyclic voltammetry measurements, which provide further characterization of the electrochemical response and are in line with the above discussion.

Transient Absorbance Spectroscopy−300 nm Pump. Figure 7 reports FTAS spectra measured at increasing delay
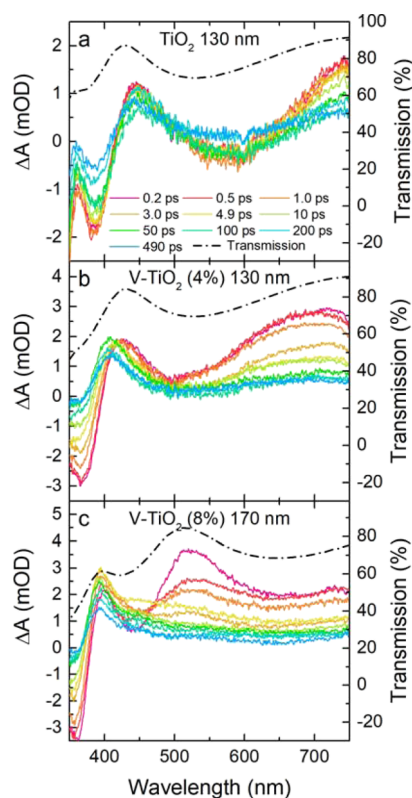

Figure 7. FTAS spectra of (a) TiO₂ and (b,c) V−TiO₂ thin films at increasing delay times after photoexcitation at 300 nm. The dashed lines, referred to the right axis, report the corresponding static transmission spectra.

times following excitation at $\lambda_e = 300$ nm, that is, with a photon energy above the anatase band gap (≈390 nm). The first noticeable feature common to all samples is the negative transient signal in the short wavelength part of the spectra, with a minimum at ≈390 nm in TiO₂ and at ≈360 nm in V−TiO₂ due to the bleaching of the band gap.

In the longer wavelength region ($\lambda_p > 450$ nm), the line shape of FTAS spectra is quite similar to the static absorbance spectra, reported as dashed lines in Figure 7, whose maxima and minima

are due to interference effects and depend on film thickness. In other words, the FTAS spectra appear to be modulated by the interference effects also observed in static spectra. In the Supporting Information, we report simulations[38] of the static spectra, which support this interpretation (see Figure S7, Table S5). Such modulations of the FTAS spectra have been previously observed in TiO$_2$ films[39] and suggest that the signal is strongly affected by changes in the interference pattern brought about by a photoinduced modulation of the refractive index. Interference fringes in pump−probe optical measurements were also observed in silicon thin films for photovoltaic applications.[40] The change of the refractive index depends on the polarizability and the density of free carriers, and thus, we interpret this time-dependent signal to be a measurement of the density of free carriers. This method has been applied recently to investigate free carrier dynamics in thin films of metal halide perovskites.[41] It is worth to emphasize that such modulations were not observed in our previous work on nanoparticle-assembled porous TiO$_2$ films, where the FTAS spectra exhibited a gradually rising intensity to a higher wavelength.[16] This difference is clearly due to the absence of interference fringes in rough mesoporous films, in agreement with previous studies.[39]

Even though the FTAS spectra are modulated by interference effects, the evolution as a function of time in the region $\lambda_p > 600$ nm is a representative of the dynamics of both free and trapped electrons, as amply reported and discussed in the literature.[5,16,28,39] The contribution of the free electron signal increases approximately as $\lambda_p^{1.7}$, while trapped electrons usually give FTAS bands centered in the range of 600−800 nm.[22] It is not possible to separate the two contributions without performing measurements in a much wider spectral range. Therefore, in the following, we will refer to the FTAS signal at $\lambda_p > 600$ nm simply as the E signal. We note that it is the free electrons that contribute to the photoelectrochemical reaction because they can flow into the external circuit. The spectra reported in Figure 7 clearly show that the E signal decays more slowly in unmodified TiO$_2$ compared to that in V−TiO$_2$, hinting at a faster recombination dynamics induced by V incorporation; this feature will be discussed in the next section.

The signature of THs, in the form of a band centered around $\lambda_p \approx 400$ nm, becomes clearly visible in the modified films at long delay times (>50 ps) in which the amplitude of the E signal is very small. The assignment of FTAS bands centered at 400−500 nm to surface-THs is well established for nanostructured TiO$_2$[5,22] and was also observed in our previous study on nanoparticle-assembled V−TiO$_2$ films.[16] In the unmodified TiO$_2$ film, the long-living modulated electron signal along with the photoinduced bleaching effect of the band edge tends to obscure the TH feature. The analysis of the hole dynamics and its decoupling from interference effects will be presented after the discussion of the electron dynamics. Before discussing electron and hole dynamics in detail, we note that the presence of interference effects can explain, at least partially, the blue shift of the band gap bleaching signal (350−400 nm) induced by V incorporation. In fact, as can be seen from the dashed lines in Figure 7, the static transmission spectra themselves blue-shift, giving rise to the shift of the transient band gap bleaching feature.

Electron Dynamics. Following the reasoning outlined above, for the analysis of the electron dynamics, we inspect the time evolution of the E signal at $\lambda_p = 710$ nm, that is, far enough from the TH band at $\lambda_p \approx 400$ nm to exclude superposition of these features. The measured time traces,

normalized to a common maximum value for the sake of comparison, are reported in Figure 8a,b for the unmodified and
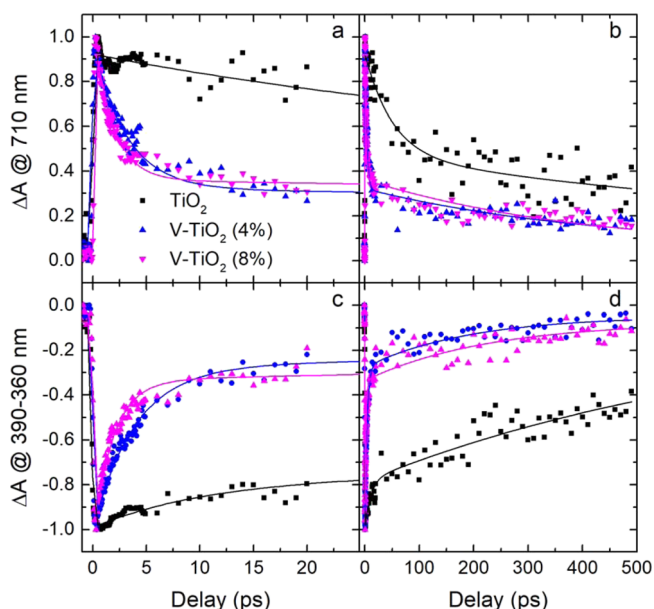

Figure 8. Normalized time traces following 300 nm excitation taken at (a,b) $\lambda_p = 710$ nm and (c,d) $\lambda_p = 390 − 360$ nm. The solid lines display the best fit according to the double exponential function reported in eq 3. Short time delays are reported on the left and longer ones on the right.

the two V−TiO$_2$ films. The solid lines represent the best fits of the time traces to the sum of one exponential rise and two exponential decay functions convolved with a Gaussian-shaped IRF

$$\Delta A(t) = \sum_{i=1,2} A_i \frac{\tau_i}{(\tau_r - \tau_i)} \left(e^{\sigma^2/2\tau_r^2 - t/\tau_r} \right.$$
$$\left(1 + \mathrm{erf}\left(\frac{t}{\sqrt{2}\,\sigma} - \frac{\sigma}{\sqrt{2}\,\tau_i} \right) \right) - e^{\sigma^2/2\tau_i^2 - t/\tau_i}$$
$$\left. \left(1 + \mathrm{erf}\left(\frac{t}{\sqrt{2}\,\sigma} - \frac{\sigma}{\sqrt{2}\,\tau_i} \right) \right) \right) \tag{3}$$

in which A_i is the amplitude of the ith component, τ_i is the corresponding decay time, τ_r is the rise time, and $\sigma = 30$ fs is the standard deviation of the Gaussian laser pump.

It is interesting to compare the temporal trend of the E signal with the recovery of the band gap bleaching, represented by the time evolution of the (negative) transient amplitude at $\lambda_p = 360$ nm, as reported in Figure 8c,d. The best-fit parameters obtained for the E signal and the bleaching are summarized in Table 1. In both cases, the fast rise time, compared to the IRF (≈ 80 fs), is due to the effects of thermalization of the initially excited carriers. This indicates that the E signal in the first few picoseconds is mainly due to free electrons in the bulk because the characteristic times for electron diffusion and trapping at the surface are much longer (≈ 10 ps), even for small nanoparticles with a diameter of 12 nm.[16] V-incorporation significantly speeds up the decay of both signals, as is evident in Figure 8. In particular, for the E signal, the decay time τ_1 of the fastest decaying component decreases from 51 ps in pure TiO$_2$ to 3.1 ps

F

Table 1. Amplitude, Rise and Decay Time of the E (λ_p = 710 nm), and Bleaching (λ_p = 390−370 nm) Signals Obtained from the Fit with eq 3. The Thickness d of the Films is also Reported

	TiO$_2$		V−TiO$_2$ (4%)		V−TiO$_2$ (8%)	
d (nm)	130 ± 5		130 ± 5		170 ± 5	
λ_p	390 nm	710 nm	360 nm	710 nm	360 nm	710 nm
A_1	−0.21(2)	0.45(0.05)	−0.72(0.02)	0.66(0.02)	−0.69(0.02)	0.65(0.02)
A_2	−0.72(0.02)	0.40(0.06)	−0.23(0.02)	0.26(0.02)	−0.26(0.01)	0.32(0.01)
τ_r (fs)	83(13)	88(17)	81(10)	68(11)	69(11)	45(10)
τ_1 (ps)	10(2)	50(10)	3.9(0.2)	3.1(0.2)	1.9(0.1)	1.8(0.1)
τ_2 (ps)	720(50)	1000(400)	190(30)	420(60)	220(30)	410(40)

at 4% incorporation and to 1.8 at 8% incorporation. Table 1 shows a very good match between the τ_1 values obtained for the E and bleaching signals in the case of V-modified samples. For pure TiO$_2$, the two values show a larger spread because of the analysis of the bleaching signal that is more problematic with respect to the modified samples because it strongly overlaps with the TH band. Because the bleaching recovers via electron−hole recombination, the similar decay dynamics hints at electron−hole recombination as the dominant mechanism for the decay of the E signal. The detected dependence of τ_1 on the V incorporation level indicates that V dopants act as recombination centers. This finding agrees with the observed fast decay of the E signal in TiO$_2$ nanoparticles, for which it was found that V incorporation accelerates recombination.[16] In addition, this can explain the evidence from photoelectrochemistry measurements that under UV irradiation (λ_e = 300 nm), V incorporation proves to be detrimental for photoelectrocatalysis because it accelerates the recombination of electrons generated in the bulk, reducing the probability to reach the FTO substrate and to be injected in the external circuit.

The slower exponential decay of the E signal with the characteristic time τ_2 in the 100 s of the picosecond range is usually associated with the relaxation of free electrons and shallowly traps electrons into deep traps, which are optically inactive.[42] The τ_2 value obtained here ($\approx$1000 ps for TiO$_2$ and $\approx$400 ps for V−TiO$_2$) is larger than that of nanoparticle-assembled films ($\approx$200 ps).

Hole Dynamics in V-Modified Samples. In order to decouple the electron and hole dynamics and to recover the time dependence of the TH band at short delays, in which interference effects and bleaching are quite strong, we fit the FTAS spectra as the superposition of two components. The first component, associated with the interference-modulated E signal and the bleaching, dominates at very short time delays. The second component is associated with the TH band at 400 nm, which becomes evident in the spectra of the V-modified films after 100 ps. Therefore, in order to represent the first component, we chose the FTAS spectrum $\Delta A(0.2)$ measured after 0.2 ps, which minimizes the presence of the TH signal. The TH signal, with minimal distortions due to interference and bleaching, was taken as the FTAS spectrum $\Delta A(450)$ measured at a time delay of 450 ps. The temporal evolution of the TA spectra $\Delta A(t)$ was fitted as a linear combination of these two components with time-dependent coefficients $e(t)$ and $h(t)$ according to

$$\Delta A(t) = e(t) \times \Delta A(0.2) + h(t) \times \Delta A(450) \qquad (4)$$

The values of the coefficients $e(t)$ and $h(t)$ were obtained through the Levenberg−Marquardt algorithm by minimizing the difference between the experimental spectrum and the linear combination as per eq 4. The outcome of this procedure is

illustrated in Figure 9 for the FTAS spectrum at a delay time of 4.9 ps measured on V−TiO$_2$ (4%). Further data for all samples and different delay times are reported in Figure S8.
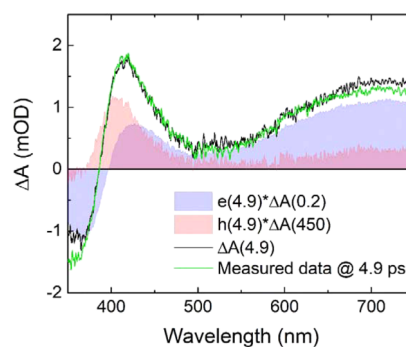

Figure 9. Example of the fitting procedure with eq 4 used for extracting the hole signal from sample V−TiO$_2$ (4%) with a delay time of 4.9 ps.

The temporal evolution of the $e(t)$ coefficient is reported in Figure S9. Because $e(t)$ carries a strong contribution from both the interference-modulated E signal and the bleaching signal, its time dependence is expected to be very similar to the one discussed above for the time traces at λ_p = 710 nm. This is indeed the case, as shown in Figure S9. In fact, by fitting $e(t)$ to the double exponential decay function eq 3, we obtain the decay times listed in Table S6 that are in good agreement with those of the E and bleaching signals (Table 1). This overall consistency supports the validity of our approach.

The temporal dynamics of THs, described by the $h(t)$ coefficient, is displayed in Figure 10. One can see that the TH signal rises within the first few picoseconds and then remains almost constant. The rise time τ_r can be determined by fitting
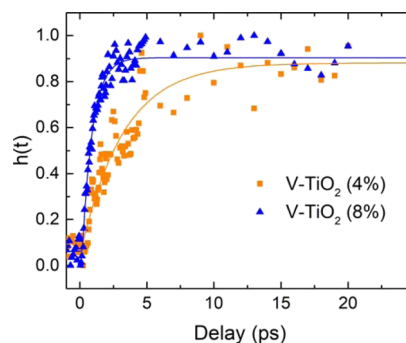

Figure 10. Time dependence of the $h(t)$ coefficients with relative fits; time traces have been normalized to unity at long delay times. A plot over a longer delay interval is reported in the Supporting Information, as shown in Figure S10.

$h(t)$ to an IRF, which corresponds to eq 3 without exponential decay. The best-fit parameters for the amplitude and rise time of the TH signal are reported in Table 2.

Table 2. Amplitude and Rise Time of the TH Signal Obtained by Fitting $h(t)$ to eq 4 without the Exponential Decay. l Is the Mean Distance Traveled by Holes in the Time τ_r

	V–TiO$_2$ (4%)	V–TiO$_2$ (8%)
A_1	0.78(0.02)	0.84(0.02)
τ_r (ps)	3.2(0.3)	0.77(0.05)
l (nm)	11	6

The rise time of the TH signal in V-modified thin films, 3.2 ps for 4% V-incorporation and 0.77 ps for 8% V-incorporation, is much larger than the value $\tau_r \approx 250$ fs measured in mesoporous films constituted by aggregated nanoparticles with a mean diameter of about 12 nm.[16] Considering that holes are mostly trapped at the surface or subsurface sites,[5] this difference can be ascribed to the different morphology of the systems. In fact, the mean distance traveled by holes in the time τ_r is

$$l = \sqrt{D_{\text{hole}} \tau_r} \tag{5}$$

in which $D_{\text{hole}} = 4 \times 10^{-5}$ m^2/s is the hole diffusion coefficient in TiO$_2$[43] and l is 11 and 6 nm for 4 and 8% V-incorporation, respectively, also reported in Table 2. These distances are much smaller than the film thicknesses (130 and 170 nm), but they are comparable to the penetration depth δ of UV radiation at $\lambda_e = 300$ nm. In fact, $\delta = \lambda_e/4\pi n_2$ (with n_2, the imaginary part of the refractive index, taken from refs 44 and 45) ranges between 27 and 40 nm; this limits the absorption of incoming photons, and as a consequence the generation of holes, within this distance from the surface. We also note that l is similar to the hole diffusion length in single-crystal TiO$_2$, $l_{\text{TiO}_2} \approx 10$ nm.[46] In conclusion, we have $l \cong l_{\text{TiO}_2} < \delta$, which suggests that most holes are excited within 30–40 nm from the surface, but only those closer than 10–15 nm have a high probability to eventually reach the surface traps. A sketch of the entire process is displayed in Figure 11.
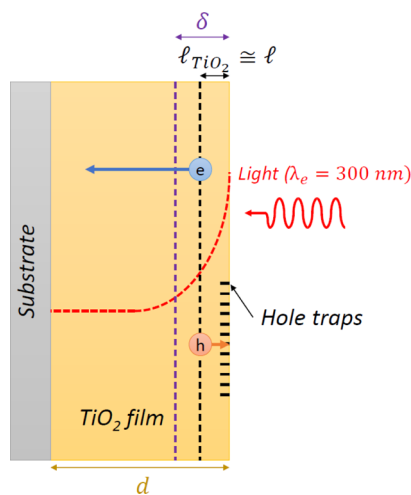

Figure 11. Illustration of the generation and trapping process for holes with a pump at 300 nm. The red line represents the exponentially decaying light intensity inside the film.

On the basis of this picture, we can provide an explanation of the observed results concerning the hole dynamics. The much shorter rise time of the TH hole signal in nanoparticle-assembled films[16] with respect to the present case derives from the proximity of the nanoparticle surface to the hole generation site. The shorter distance traveled by holes in V–TiO$_2$ (8%) with respect to the 4% incorporation level can be correlated with the faster decay of the E signal due to recombination, as discussed previously. In other words, the accelerated recombination induced by V incorporation reduces the average distance that a free hole can travel before being trapped. On the other hand, the dynamics of surface-THs and free electrons are clearly uncorrelated at long delay times: the former live without significant decay up to 100 ps (see Figure S10), while for the latter only 30% of the signal survives after 100 ps, further decreasing to 20% after 500 ps. Such decoupling suggests that free electrons mainly recombine with holes that do not contribute to the TA signal in the measured spectral range.

Hole Dynamics: Unmodified Sample. We have not succeeded in extracting the time dynamics of the THs in the case of the pure TiO$_2$ sample because of the combination of two factors. First, the shift to higher energies of the TH absorption band in TiO$_2$ in comparison with that in the modified samples leads to a stronger overlap with the band gap bleaching signal. Second, the longer lifetimes of the electrons in the pure sample make it very difficult to isolate the TH absorption band at long delay times. Nonetheless, a stronger positive contribution at 360 nm was observed at long delay times with respect to short times, suggesting that the TH is absorbed in this region in pure TiO$_2$.

Pump at 390 and 530 nm. FTAS spectra with $\lambda_e = 390$ and 530 nm are shown in Figure 12. At these wavelengths, we had to
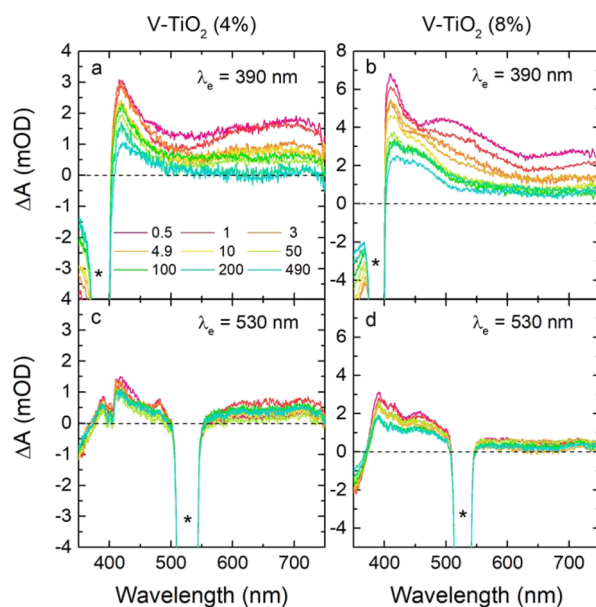

Figure 12. FTAS spectra of V–TiO$_2$ 4 and 8% films with a pump at 390 nm (top) and at 530 nm (bottom). The symbol * marks the negative signal because of scattering of the pump light into the detector.

increase the intensity of the pump pulse up to 2 mJ/cm^2 in order to obtain a spectrum with a good signal-to-noise ratio. However, at such a high intensity, the dynamics of charge carriers can be affected by higher-order relaxation processes, such as Auger recombination, which involves a nonradiative energy transfer between several charge carriers.[47] As a consequence, we will

discuss the line shape of the spectra without analyzing its dynamics.

No transient signal was measured in pure TiO_2 because this sample is completely transparent at either of these pump wavelengths. This is consistent with the lack of photo-electrocatalysis for the unmodified sample in the visible range above 390 nm, as previously discussed in point (ii) of the Photoelectrochemistry section. Instead, it is evident from Figures 12a,b that with λ_e = 390 nm, V-modified samples still show the E signal modulated by interference fringes and the long-living TH signal at 400−500 nm (the negative signals at 390 are due to the pump pulse). The intensity of the E signal with respect to the TH signal is lower than with λ_e = 300 nm. Finally, with λ_e = 530 nm (Figure 11c,d), the TH signal remains clearly visible and the modulated E signal becomes barely detectable (note that in this case, the negative signals at 530 nm are due to the pump pulse). These results can be related to the photoelectrochemistry of the system. In particular, it is worth noticing that the TH signal intensity of V−TiO_2 (8%) is about twice that found in the 4% modified film, both at λ_e = 390 and 530 nm, explaining the higher conversion efficiency of the former sample. The photocatalytic activity in the visible range, mentioned in the Photoelectrochemistry Section, indeed relies on the presence of charge carriers that replicate the same dynamics seen in the UV range. Recalling that the energy gap of anatase TiO_2 is equivalent to a wavelength of 390 nm, this means that it is possible to generate free electrons in the conduction band (E signal) with an energy lower than the energy gap, down to at least 2.3 eV (= 530 nm). As shown in our previous paper, on V−TiO_2 nanoparticles,[16] these electrons most likely come from V donor sites located within the band gap of TiO_2. Photo-electrochemistry measurements show a photocatalytic activity that extends up to ≈550 nm, which implies that V levels are located at ≈2.2 eV below the bottom of the conduction band.

CONCLUSIONS

In this paper, we showed how the introduction of substitutional V in TiO_2 thin films can modify the transient optical absorption and photoelectrocatalytic activity. Femtosecond transient absorbance spectroscopy provided the basis to interpret the results of the photoelectrochemistry measurements. The introduction of vanadium allows TiO_2 to exhibit water-splitting activity in the visible spectral region where normally it is inactive; on the other hand, it negatively affects the energy conversion performance in the UV range. Light absorption and charge transport are the upstream processes of photo-electrocatalysis, and in fact, they undergo significant alterations because of vanadium incorporation. In particular, we found that

i Light absorption is extended from UV (390 nm, the band gap of anatase TiO_2) up to ≈530 nm in the visible range, as shown by the presence of a TA signal after excitation at 530 nm. Following the results reported in our previous article about TiO_2 nanoparticles, this is most probably related to the introduction of donor levels associated with V sites inside the TiO_2 energy gap. From these occupied intragap states, electrons can be photoexcited in the conduction band even upon subband gap irradiation. By comparing photoelectrochemistry and TA measurements, a reasonable upper limit for the distribution of V energy levels within the TiO_2 energy gap can be set at ≈2.2 eV below the bottom of the conduction band.

ii Charge dynamics is influenced by V as well. We showed that V accelerates electron−hole recombination in the modified samples upon UV irradiation. This side effect is probably responsible for decreasing considerably the conversion efficiency in this spectral range.

iii Photoelectrocatalysis in the visible range is related to free electrons and THs coming from V donor sites in the TiO_2 energy gap.

The linear combination procedure suggested to decouple the E signal from the TH signal proved to be effective in recovering the rising time of the THs, showing that there is no recombination between free electrons in the bulk and THs on the surface because they live much more than electrons.

Future studies could investigate the behavior of different metallic dopants, such as Cr, Co, Fe, and so forth, or nonmetallic ones such as N or C, in terms of both energy levels and fast time dynamics, in order to determine systematically how they can modify the photoelectrocatalytic activity of TiO_2.

ASSOCIATED CONTENT

ⓢ Supporting Information

The Supporting Information is available free of charge at https://pubs.acs.org/doi/10.1021/acs.jpcc.0c06790.

Sputtering cathode; (101) lattice spacing and crystallite size determined from XRD; Raman peak positions and widths; details of the IRF in the FTAS measurements; details on the XPS data analysis containing survey XPS spectra; XPS spectra of Ti 2p, O 1s, and C 1s core levels; electrochemical impedance spectroscopy and cyclic voltammetry measurements with analysis and discussion; details on the simulations of the static optical transmission spectra reporting the comparison between experimental and simulated spectra; thickness and roughness of the films; and analysis of the FTAS spectra (PDF)

AUTHOR INFORMATION

Corresponding Author

Federico Boscherini − *Department of Physics and Astronomy, Alma Mater Studiorum−Università di Bologna, Bologna 40127, Italy;* ⓞ orcid.org/0000-0002-9703-3903; Email: federico.boscherini@unibo.it

Authors

Alberto Piccioni − *Department of Physics and Astronomy, Alma Mater Studiorum−Università di Bologna, Bologna 40127, Italy;* ⓞ orcid.org/0000-0002-3447-2650

Daniele Catone − *CNR-ISM, Division of Ultrafast Processes in Materials (FLASHit), Rome 00133, Italy;* ⓞ orcid.org/0000-0002-7649-2756

Alessandra Paladini − *CNR-ISM, Division of Ultrafast Processes in Materials (FLASHit), Monterotondo Scalo 00015, Italy;* ⓞ orcid.org/0000-0002-2059-1552

Patrick O'Keeffe − *CNR-ISM, Division of Ultrafast Processes in Materials (FLASHit), Monterotondo Scalo 00015, Italy;* ⓞ orcid.org/0000-0002-8676-4436

Alex Boschi − *Istituto per La Sintesi Organica e La Fotoreattività, Consiglio Nazionale Delle Ricerche, Bologna 40129, Italy; Department of Physics, Informatics and Mathematics, Università di Modena e Reggio Emilia, Modena 41125, Italy;* ⓞ orcid.org/0000-0001-7562-7340

Alessandro Kovtun − *Istituto per La Sintesi Organica e La Fotoreattività, Consiglio Nazionale Delle Ricerche, Bologna 40129, Italy;* ⓘ orcid.org/0000-0002-7614-7100

Maria Katsikini − *Department of Solid State Physics, Aristotle University of Thessaloniki, Thessaloniki 54124, Greece;* ⓘ orcid.org/0000-0002-8059-5539

Luca Pasquini − *Department of Physics and Astronomy, Alma Mater Studiorum−Università di Bologna, Bologna 40127, Italy;* ⓘ orcid.org/0000-0001-8939-2204

Complete contact information is available at:
https://pubs.acs.org/10.1021/acs.jpcc.0c06790

Author Contributions

APic. synthesized the samples, performed the photoelectrochemical measurements, and participated in the XPS and FTAS measurements. DC, APal., and POK performed the FTAS measurements. AB and AK performed the XPS measurements. MK performed the Raman measurements. FB and LP conceived this research and supervised all of its aspects. The paper is the result of a concerted action of all authors, who have given approval to the final version of the manuscript.

Notes

The authors declare no competing financial interest.

■ ACKNOWLEDGMENTS

■ REFERENCES

(1) Linsebigler, A. L.; Lu, G.; Yates, J. T., Jr Photocatalysis on TiO_2 Surfaces: Principles, Mechanisms, and Selected Results. *Chem. Rev.* **1995**, *95*, 735−758.

(2) Matsuoka, M.; Kitano, M.; Takeuchi, M.; Tsujimaru, K.; Anpo, M.; Thomas, J. M. Photocatalysis for New Energy Production. Recent Advances in Photocatalytic Water Splitting Reactions for Hydrogen Production. *Catal. Today* **2007**, *122*, 51−61.

(3) Fujishima, A.; Zhang, X.; Tryk, D. TiO_2 Photocatalysis and Related Surface Phenomena. *Surf. Sci. Rep.* **2008**, *63*, 515−582.

(4) Zhang, J. Z. Metal Oxide Nanomaterials for Solar Hydrogen Generation from Photoelectrochemical Water Splitting. *MRS Bull.* **2011**, *36*, 48−55.

(5) Schneider, J.; Matsuoka, M.; Takeuchi, M.; Zhang, J.; Horiuchi, Y.; Anpo, M.; Bahnemann, D. W. Understanding TiO_2 Photocatalysis: Mechanisms and Materials. *Chem. Rev.* **2014**, *114*, 9919−9986.

(6) Van de Krol, R.; Gratzel, M. *Photoelectrochemical Hydrogen Production*; Springer, 2012.

(7) Hashimoto, K.; Irie, H.; Fujishima, A. TiO_2photocatalysis: A Historical Overview and Future Prospects. *Japanese J. Appl. Physics, Part 1 Regul. Pap. Short Notes Rev. Pap.* **2005**, *44*, 8269−8285.

(8) Takanabe, K. Photocatalytic Water Splitting: Quantitative Approaches toward Photocatalyst by Design. *ACS Catal.* **2017**, *7*, 8006−8022.

(9) Jafari, T.; Moharreri, E.; Amin, A. S.; Miao, R.; Song, W.; Suib, S. L. Photocatalytic Water Splitting - The Untamed Dream: A Review of Recent Advances. *Molecules* **2016**, *21*, 900.

(10) Ochiai, T.; Fujishima, A. Photoelectrochemical Properties of TiO_2 Photocatalyst and Its Applications for Environmental Purification. *J. Photochem. Photobiol. C Photochem. Rev.* **2012**, *13*, 247−262.

(11) O'Regan, B.; Grätzel, M. A Low-Cost, High-Efficiency Solar Cell Based on Dye-Sensitized Colloidal TiO_2 Films. *Nature* **1991**, *353*, 737−740.

(12) Amidani, L.; Naldoni, A.; Malvestuto, M.; Marelli, M.; Glatzel, P.; Dal Santo, V.; Boscherini, F. Probing Long-Lived Plasmonic-Generated Charges in TiO_2/Au by High-Resolution x-Ray Absorption Spectroscopy. *Angew. Chem. Int. Ed.* **2015**, *54*, 5413−5416.

(13) Peeters, H.; Keulemans, M.; Nuyts, G.; Vanmeert, F.; Li, C.; Minjauw, M.; Detavernier, C.; Bals, S.; Lenaerts, S.; Verbruggen, S. W. Plasmonic Gold-Embedded TiO_2 Thin Films as Photocatalytic Self-Cleaning Coatings. *Appl. Catal. B Environ.* **2020**, *267*, 118654.

(14) Cristino, V.; Pasti, L.; Marchetti, N.; Berardi, S.; Bignozzi, C. A.; Molinari, A.; Passabi, F.; Caramori, S.; Amidani, L.; Orlandi, M.; et al. Photoelectrocatalytic degradation of emerging contaminants at WO3/BiVO4 photoanodes in aqueous solution. *Photochem. Photobiol. Sci.* **2019**, *18*, 2150−2163.

(15) Zhang, H.; Chen, G.; Bahnemann, D. W. Photoelectrocatalytic Materials for Environmental Applications. *J. Mater. Chem.* **2009**, *19*, 5089−5121.

(16) Rossi, G.; Pasquini, L.; Catone, D.; Piccioni, A.; Patelli, N.; Paladini, A.; Molinari, A.; Caramori, S.; O'Keeffe, P.; Boscherini, F. Charge Carrier Dynamics and Visible Light Photocatalysis in Vanadium-Doped TiO_2 Nanoparticles. *Appl. Catal. B Environ.* **2018**, *237*, 603−612.

(17) Rossi, G.; Calizzi, M.; Di Cintio, V.; Magkos, S.; Amidani, L.; Pasquini, L.; Boscherini, F. Local Structure of V Dopants in TiO_2 Nanoparticles: X-Ray Absorption Spectroscopy, Including Ab-Initio and Full Potential Simulations. *J. Phys. Chem. C* **2016**, *120*, 7457−7466.

(18) Rossi, G.; Calizzi, M.; Amidani, L.; Migliori, A.; Boscherini, F.; Pasquini, L. Element-Specific Channels for the Photoexcitation of V-Doped TiO_2 Nanoparticles. *Phys. Rev. B* **2017**, *96*, 45303.

(19) Umebayashi, T.; Yamaki, T.; Itoh, H.; Asai, K. Analysis of Electronic Structures of 3d Transition Metal-Doped TiO_2 Based on Band Calculations. *J. Phys. Chem. Solids* **2002**, *63*, 1909−1920.

(20) Zhu, H. X.; Wang, X. H.; Zhou, D. F.; Jiang, H.; Liu, X. M. First-Principles Study on Electronic, Magnetic Properties and Optical Absorption of Vanadium Doped Rutile TiO_2. *Phys. Lett. A* **2020**, *384*, 126637.

(21) Baxter, J. B.; Richter, C.; Schmuttenmaer, C. A. Ultrafast Carrier Dynamics in Nanostructures for Solar Fuels. *Annu. Rev. Phys. Chem.* **2014**, *65*, 423−447.

(22) Yoshihara, T.; Katoh, R.; Furube, A.; Tamaki, Y.; Murai, M.; Hara, K.; Murata, S.; Arakawa, H.; Tachiya, M. Identification of Reactive Species in Photoexcited Nanocrystalline TiO_2 Films by Wide-Wavelength-Range (400−2500 nm) Transient Absorption Spectroscopy. *J. Phys. Chem. B* **2004**, *108*, 3817−3823.

(23) Tamaki, Y.; Furube, A.; Murai, M.; Hara, K.; Katoh, R.; Tachiya, M. Dynamics of Efficient Electron−Hole Separation in TiO_2 Nanoparticles Revealed by Femtosecond Transient Absorption Spectroscopy under the Weak-Excitation Condition. *Phys. Chem. Chem. Phys.* **2007**, *9*, 1453−1460.

(24) Tamaki, Y.; Furube, A.; Katoh, R.; Murai, M.; Hara, K.; Arakawa, H.; Tachiya, M. Trapping Dynamics of Electrons and Holes in a Nanocrystalline TiO_2 Film Revealed by Femtosecond Visible/near-Infrared Transient Absorption Spectroscopy. *Compt. Rendus Chem.* **2006**, *9*, 268−274.

(25) Rothenberger, G.; Moser, J.; Graetzel, M.; Serpone, N.; Sharma, D. K. Charge Carrier Trapping and Recombination Dynamics in Small Semiconductor Particles. *J. Am. Chem. Soc.* **1985**, *107*, 8054−8059.

(26) Serpone, N.; Lawless, D.; Khairutdinov, R. Size Effects on the Photophysical Properties of Colloidal Anatase TiO_2 Particles: Size Quantization versus Direct Transitions in This Indirect Semiconductor? *J. Phys. Chem. A* **2002**, *99*, 16646−16654.

(27) Colombo, D. P.; Bowman, R. M. Does Interfacial Charge Transfer Compete with Charge Carrier Recombination? A Femtosecond Diffuse Reflectance Investigation of TiO_2 Nanoparticles. *J. Phys. Chem.* **1996**, *100*, 18445−18449.

(28) Nunzi, F.; De Angelis, F.; Selloni, A. Ab Initio Simulation of the Absorption Spectra of Photoexcited Carriers in TiO_2 Nanoparticles. *J. Phys. Chem. Lett.* **2016**, *7*, 3597−3602.

(29) O'Keeffe, P.; Catone, D.; Paladini, A.; Toschi, F.; Turchini, S.; Avaldi, L.; Martelli, F.; Agresti, A.; Pescetelli, S.; Del Rio Castillo.; et al.

Graphene-Induced Improvements of Perovskite Solar Cell Stability: Effects on Hot-Carriers. *Nano Lett.* **2019**, *19*, 684−691.

(30) Stagi, L.; Carbonaro, C. M.; Corpino, R.; Chiriu, D.; Ricci, P. C. Light Induced TiO$_2$ Phase Transformation: Correlation with Luminescent Surface Defects. *Phys. Status Solidi Basic Res.* **2015**, *252*, 124−129.

(31) Alhomoudi, I. A.; Newaz, G. Residual Stresses and Raman Shift Relation in Anatase TiO2 Thin Film. *Thin Solid Films* **2009**, *517*, 4372−4378.

(32) El Koura, Z.; Rossi, G.; Calizzi, M.; Amidani, L.; Pasquini, L.; Miotello, A.; Boscherini, F. XANES Study of Vanadium and Nitrogen Dopants in Photocatalytic TiO$_2$ Thin Films. *Phys. Chem. Chem. Phys.* **2018**, *20*, 221−231.

(33) Zhu, K.-R.; Zhang, M.-S.; Chen, Q.; Yin, Z. Size and Phonon-Confinement Effects on Low-Frequency Raman Mode of Anatase TiO2 Nanocrystal. *Phys. Lett. A* **2005**, *340*, 220−227.

(34) Barreca, D.; Gasparotto, A.; Maccato, C.; Maragno, C.; Tondello, E. TiO$_2$ Thin Films by Chemical Vapor Deposition: An XPS Characterization. *Surf. Sci. Spectra* **2007**, *14*, 27−33.

(35) Stoch, J.; Gablankowska-Kukucz, J. The Effect of Carbonate Contaminations on the XPS O 1s Band Structure in Metal Oxides. *Surf. Interface Anal.* **1991**, *17*, 165−167.

(36) Yan, J.; Wu, G.; Guan, N.; Li, L.; Li, Z.; Cao, X. Understanding the Effect of Surface/Bulk Defects on the Photocatalytic Activity of TiO$_2$: Anatase versus Rutile. *Phys. Chem. Chem. Phys.* **2013**, *15*, 10978−10988.

(37) Silversmit, G.; Depla, D.; Poelman, H.; Marin, G. B.; De Gryse, R. Determination of the V 2p XPS Binding Energies for Different Vanadium Oxidation States (V^{5+} to V^{0+}). *J. Electron Spectrosc. Relat. Phenom.* **2004**, *135*, 167−175.

(38) Centurioni, E. Generalized Matrix Method for Calculation of Internal Light Energy Flux in Mixed Coherent and Incoherent Multilayers. *Appl. Opt.* **2005**, *44*, 7532.

(39) Sachs, M.; Pastor, E.; Kafizas, A.; Durrant, J. R. Evaluation of Surface State Mediated Charge Recombination in Anatase and Rutile TiO$_2$. *J. Phys. Chem. Lett.* **2016**, *7*, 3742−3746.

(40) Moon, J. A.; Tauc, J. Interference Effects in Pump-Probe Spectroscopy of Thin Films. *J. Appl. Phys.* **1993**, *73*, 4571−4578.

(41) Pasanen, H. P.; Vivo, P.; Canil, L.; Abate, A.; Tkachenko, N. Refractive Index Change Dominates the Transient Absorption Response of Metal Halide Perovskite Thin Films in the near Infrared. *Phys. Chem. Chem. Phys.* **2019**, *21*, 14663−14670.

(42) Tamaki, Y.; Furube, A.; Murai, M.; Hara, K.; Katoh, R.; Tachiya, M. Dynamics of Efficient Electron-Hole Separation in TiO$_2$ Nano-particles Revealed by Femtosecond Transient Absorption Spectroscopy under the Weak-Excitation Condition. *Phys. Chem. Chem. Phys.* **2007**, *9*, 1453−1460.

(43) Enright, B.; Fitzmaurice, D. Spectroscopic Determination of Electron and Hole Effective Masses in a Nanocrystalline Semi-conductor Film. *J. Phys. Chem.* **1996**, *100*, 1027−1035.

(44) Siefke, T.; Kroker, S.; Pfeiffer, K.; Puffky, O.; Dietrich, K.; Franta, D.; Ohlídal, I.; Szeghalmi, A.; Kley, E. B.; Tünnermann, A. Materials Pushing the Application Limits of Wire Grid Polarizers Further into the Deep Ultraviolet Spectral Range. *Adv. Opt. Mater.* **2016**, *4*, 1780−1786.

(45) Sarkar, S.; Gupta, V.; Kumar, M.; Schubert, J.; Probst, P. T.; Joseph, J.; König, T. A. F. Hybridized Guided-Mode Resonances via Colloidal Plasmonic Self-Assembled Grating. *ACS Appl. Mater. Interfaces* **2019**, *11*, 13752−13760.

(46) Salvador, P. Hole Diffusion Length in N-TiO$_2$ Single Crystals and Sintered Electrodes: Photoelectrochemical Determination and Comparative Analysis. *J. Appl. Phys.* **1984**, *55*, 2977−2985.

(47) Maity, P.; Mohammed, O. F.; Katsiev, K.; Idriss, H. Study of the Bulk Charge Carrier Dynamics in Anatase and Rutile TiO$_2$ Single Crystals by Femtosecond Time-Resolved Spectroscopy. *J. Phys. Chem. C* **2018**, *122*, 8925−8932.

K